Analysis and direct numerical simulation of the flow at a gravity-current head. Part 1. Flow topology and front speed for slip and no-slip boundaries

By CARLOS HÄRTEL, ECKART MEIBURG†
AND FRIEDER NECKER

Swiss Federal Institute of Technology, Institute of Fluid Dynamics, ETH Zentrum,
CH-8092 Zürich, Switzerland

Direct numerical simulations are performed of gravity-current fronts in the lock-exchange configuration. The case of small density differences is considered, where the Boussinesq approximations can be adopted. The key objective of the investigation is a detailed analysis of the flow structure at the foremost part of the front, where no previous high-resolution data were available. For the simulations, high-order numerical methods are used, based on spectral and spectral-element discretizations and compact finite differences. A three-dimensional simulation is conducted of a front spreading along a no-slip boundary at a Reynolds number of about 750. The simulation exhibits all features typically observed in experimental flows near the gravity-current head, including the lobe-and-cleft structure at the leading edge. The results reveal that the flow topology at the head differs from what has been assumed previously, in that the foremost point is not a stagnation point in a translating system. Rather, the stagnation point is located below and slightly behind the foremost point in the vicinity of the wall. The relevance of this finding for the mechanism behind the lobe-and-cleft instability is discussed. In order to explore the high-Reynolds-number regime, and to assess potential Reynolds-number effects, two-dimensional simulations are conducted for Reynolds numbers up to about 30 000, for both no-slip and slip (i.e. shear-stress free) boundaries. It is shown that although quantitative Reynolds-number effects persist over the whole range examined, no qualitative changes in the flow structure at the head can be observed. A comparison of the two-dimensional results with laboratory data and the three-dimensional simulation provides evidence that a two-dimensional model is able to capture essential features of the flow at the head. The simulations also show that for the free-slip case the shape of the head agrees closely with the classical inviscid theory of Benjamin.

1. Introduction

Gravity currents are essentially horizontal flows driven by the differences in hydrostatic pressure at a lateral boundary between a lighter and a heavier fluid. In atmospheric gravity currents, such as sea-breeze fronts or thunderstorm outflows, the density differences are typically caused by temperature differences between the

† Permanent address: Department of Mechanical and Environmental Engineering, University of California, Santa Barbara, CA 93106, USA.

spreading cold front and the relatively warmer ambient air. In other applications, density differences may have other sources such as inhomogeneities in the distribution of a dissolved substance (such as salt in oceanic flows), or the presence of a heavier particulate phase, as in powder-snow avalanches. Gravity currents are most commonly encountered in geophysical applications (see Simpson 1997; Huppert 1986), but their dynamical evolution is of substantial interest in the engineering sciences also, due to the important role they play in many problems related to industrial safety and environmental protection (see Fanneløp 1994). A typical scenario in which gravity currents can form is the accidental release of dense industrial gases that gravity may spread over relatively large distances at an appreciable speed. A detailed account of the great diversity of gravity currents, and of their relevance in the natural sciences and engineering, is given in the monograph of Simpson (1997).

The interest in gravity currents from the various disciplines has initiated a substantial amount of theoretical and experimental research in which gravity currents were often investigated under idealized conditions that allow the various mechanisms to be addressed in a more isolated fashion. For example, much work has focused on gravity currents in confined geometries such as channels and pipes, or on the spreading of dense fluids over horizontal and inclined plane surfaces (see e.g. Benjamin 1968; Britter & Simpson 1978; Gröbelbauer, Fanneløp & Britter 1993; Hallworth *et al.* 1996; Huppert 1982; Klemp, Rotunno & Skamarock 1994; Simpson & Britter 1979; Yao & Lundgren 1996). These studies have shown that the dynamics of gravity currents can to a large extent be understood on the basis of shallow-water theory, provided that accurate hydraulic front conditions are available for the non-hydrostatic flow at the head of the current. However, concerning the flow at the head, there are still several unresolved questions regarding, for example, the nature of the instability that leads to the pronounced lobe-and-cleft structure at the leading edge of gravity currents spreading along solid boundaries. In this respect, highly resolved numerical simulations can be expected to provide useful information. Efforts to use numerical investigations as a complementary tool to experimental measurements in gravity-current research date back over two decades. However, previous computational studies employed rather coarse computational grids, in combination with low-order integration schemes, and were not able to resolve the entire range of length scales present in the flow (see e.g. Haase & Smith 1989; Jacobsen & Magnussen 1987; Kao, Park & Pao 1977; Klemp *et al.* 1994; Thorpe, Miller & Moncrieff 1980; Wang 1985). Therefore, empirical models and/or additional numerical damping terms had to be used, in order to mimic the unresolved transport processes. Direct numerical simulations (DNS) of gravity currents, which are simulations in which all scales of motion are fully resolved in space and time, have not been attempted to date.

In the present investigation, which is composed of two parts, we discuss results of a DNS study of gravity currents, which we conducted in order to clarify some of the open questions concerning the flow at the head of intrusion fronts. Part 1 is concerned with the topology of the flow at the leading edge and in the near-wall region, which we examine under different types of boundary conditions beneath the front, namely rigid no-slip walls and free-slip (i.e. shear-stress free) boundaries. This flow region could not be analysed in detail in the past, due to a lack of resolution of the data available from either experiments or computations. Clearly, knowledge of the topology at the head of a gravity current is a prerequisite for any theoretical treatment of the flow. Previous theoretical approaches often had to rely on *ad-hoc* assumptions about the flow within the gravity-current head, a common assumption being that the nose of the front (the foremost point) is a stagnation point in a translating system moving
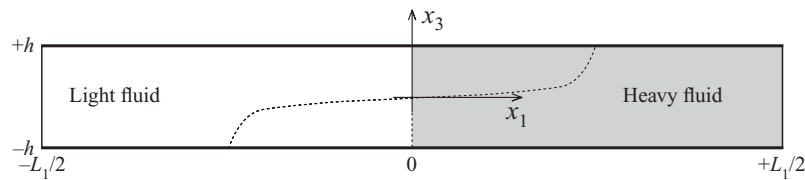
FIGURE 1. Lock-exchange flow in a channel of length L_1 and height $2h$. The dotted line gives the interface between the two fluids some time after the release (gravity acts in the normal direction x_3).

with the front (see Simpson & Britter 1979). The DNS results to be discussed in §4 reveal that, for no-slip walls, stagnation point and nose are in fact distinct. Among other things, this finding has relevance for the stability of the flow at the leading edge of the front and, hence, for the lobe-and-cleft structure. In Part 2 of the present work (Härtel, Carlsson & Thunblom 2000) we will address this point in detail, and we will employ DNS along with linear-stability theory to clarify the hydrodynamic instability which is responsible for the lobe formation at a gravity-current head.

The configuration we consider is the lock-exchange flow, a prototype problem that has been extensively investigated in experiments in the past (see Fanneløp 1994; Simpson 1997). Laboratory lock-exchange flows are usually generated in a plane channel filled with two fluids of different density, which are initially separated by a vertical gate (see figure 1). When the gate is withdrawn, a mutual intrusion flow develops, which is characterized by a pair of fronts that travel in opposite directions. The lock-exchange configuration is particularly well-suited to study the flow at the head in detail, because in this flow the developed fronts propagate at essentially constant speed after a short initial transient (see e.g. Härtel, Meiburg & Necker 1999). This allows the head of the front to be examined under steady-state conditions by using a translating reference frame in which the foremost part is at rest and the flow around it essentially stationary.

In the following, we will present results from a three-dimensional simulation that exhibits all the characteristic features of gravity currents, including the pronounced lobe-and-cleft structure at the leading edge that could not be resolved in previous simulations by other authors. The Reynolds number, based on front speed and front height, is about 750, which is about a factor of 2 below the upper limit in Reynolds number that three-dimensional DNS can reach, given today's computer capabilities. This Reynolds-number restriction is caused by the fact that in DNS the numerical resolution is determined by the disparity between the largest and smallest scales, which depends directly on the ratio of inertia and viscous forces, and hence on the Reynolds number. To explore potential Reynolds-number effects and to reach the more interesting high-Reynolds-number regime, we have therefore conducted a series of two-dimensional simulations over a range of Reynolds numbers that extends to about 30 000. However, since the two-dimensional model misses the pronounced three-dimensional instabilities, a careful validation of the two-dimensional results is necessary. This will be achieved by comparison with laboratory observations and the three-dimensional simulation at lower Reynolds number. It should be stressed that a careful study of Reynolds-number effects is generally an important task in gravity-current research, since Reynolds-number limitations are not only encountered in DNS work, but also in laboratory studies where they are determined by the finite size of the apparatus and the properties of the working fluids used (see, for example, Simpson & Britter 1979, 1980 and Parsons & Garcia 1998 for a discussion of Reynolds-number

effects in experiments). If findings from laboratory studies or simulations are to be applied to large-scale flows, detailed knowledge of their dependence on Reynolds number is important.

2. Basic equations

In the present work we will focus on flows with relatively small density differences, for which the usual Boussinesq approximations can be adopted. The Boussinesq equations (cf. Gebhart *et al.* 1979), which neglect variations in density $\tilde{\rho}$ (a tilde denotes a dimensional quantity here) except for the buoyancy term of the momentum budget, are in dimensionless form

$$\frac{\partial u_k}{\partial x_k} = 0, \tag{1}$$

$$\frac{\partial u_i}{\partial t} + \frac{\partial (u_i u_k)}{\partial x_k} = -\frac{\partial p}{\partial x_i} + \frac{1}{\sqrt{Gr}}\frac{\partial^2 u_i}{\partial x_k \partial x_k} + \rho e_i^g, \tag{2}$$

$$\frac{\partial \rho}{\partial t} + \frac{\partial (\rho u_k)}{\partial x_k} = \frac{1}{\sqrt{Gr Sc^2}}\frac{\partial^2 \rho}{\partial x_k \partial x_k}. \tag{3}$$

Here u_i denotes the velocity vector, p the pressure, ρ the density, and e_i^g the unit vector in the direction of gravitational acceleration. In the present study we will consider flows in horizontal channels only, and hence $e_i^g = (0, 0, -1)^T$ generally. All terms in (1)–(3) have been made dimensionless by the channel half-height $\tilde{h}$ (see figure 1), the average density $\tilde{\rho}_a$, and the buoyancy velocity $\tilde{u}_b$

$$\tilde{u}_b = \sqrt{\tilde{g}'\,\tilde{h}}, \tag{4}$$

where $\tilde{g}'$ is the usual reduced gravity, which is computed from the gravitational acceleration $\tilde{g}$ as

$$\tilde{g}' = \tilde{g}\,\frac{\Delta\tilde{\rho}}{\tilde{\rho}_a}. \tag{5}$$

In (5), $\Delta\tilde{\rho} = \tilde{\rho}_{max} - \tilde{\rho}_{min}$ denotes the difference between the reservoir densities of light and heavy fluid, respectively. The non-dimensional pressure p and density ρ are given by

$$p = \frac{\tilde{p}}{\tilde{\rho}_a \tilde{u}_b^2}, \quad \rho = \frac{\tilde{\rho} - \tilde{\rho}_{min}}{\Delta\tilde{\rho}}. \tag{6}$$

Two dimensionless parameters arise from the normalization, the first being the ratio of buoyancy forces to viscous forces, which we will refer to as the Grashof number *Gr*

$$Gr = \left(\frac{\tilde{u}_b\,\tilde{h}}{\tilde{\nu}}\right)^2. \tag{7}$$

Equation (2) shows that the square root of the Grashof number plays the role of a Reynolds number, but for clarity we will not denote this quantity as a Reynolds number. The reason is that in virtually all experimental studies, Reynolds numbers are defined by means of the actual speed $\tilde{u}_f$ and height $\tilde{h}_f$ of the foremost part of a fully developed front, i.e.

$$Re = \frac{\tilde{u}_f \tilde{h}_f}{\tilde{\nu}}. \tag{8}$$

This definition of Re will also be adopted here. However, since both the speed and the height of the front are not known *a priori*, these quantities cannot be employed for the purpose of rendering the governing equations dimensionless. The second dimensionless parameter in the basic equations is the Schmidt number Sc, which represents the ratio of kinematic viscosity $\tilde{v}$ and molecular diffusivity $\tilde{K}$ in the density field

$$Sc = \frac{\tilde{v}}{\tilde{K}}. \tag{9}$$

Unless stated otherwise, the Schmidt number will generally be unity in the simulations discussed in this paper. If the differences in density are caused by differences in temperature, the Schmidt number Sc is identical to the Prandtl number Pr of the fluid, and the convection–diffusion equation (3) for the density variation becomes the usual budget of thermal energy.

For strictly two-dimensional flows, it is convenient to recast the governing equations in a vorticity–streamfunction formulation. Let ψ be the streamfunction and ω the spanwise vorticity, then the following relations hold:

$$\omega = \frac{\partial u_3}{\partial x_1} - \frac{\partial u_1}{\partial x_3}, \tag{10}$$

$$u_1 = \frac{\partial \psi}{\partial x_3}, \tag{11}$$

$$u_3 = -\frac{\partial \psi}{\partial x_1}. \tag{12}$$

A field equation for the vorticity is obtained by taking the curl of (2), so that the set of governing equations now becomes

$$\frac{\partial \omega}{\partial t} + u_k \frac{\partial \omega}{\partial x_k} = \frac{1}{\sqrt{Gr}} \frac{\partial^2 \omega}{\partial x_k \partial x_k} - \frac{\partial \rho}{\partial x_1}, \tag{13}$$

$$\frac{\partial^2 \psi}{\partial x_k \partial x_k} = -\omega, \tag{14}$$

$$\frac{\partial \rho}{\partial t} + \frac{\partial(\rho u_k)}{\partial x_k} = \frac{1}{\sqrt{Gr Sc^2}} \frac{\partial^2 \rho}{\partial x_k \partial x_k}. \tag{15}$$

The gravitational forcing, as expressed by the second term on the right-hand side of the vorticity equation (13), indicates that any density variation perpendicular to the direction of gravity will result in the generation of vorticity, and hence of velocity.

3. Computational approach

In the present investigation we employ two different simulation codes, the first of which is described in Härtel *et al.* (1997), where a detailed validation is also given. In both codes the governing equations are solved numerically in the rectangular domain sketched in figure 1. In principle, the problem at hand does not have any intrinsic symmetries that would allow a direct application of Fourier methods. However, if slip boundaries are introduced at $x_1 = \pm L_1/2$, a Galerkin-type discretization using sine and cosine expansions in the longitudinal direction x_1 becomes feasible. This is the approach we have adopted here, because a Fourier–Galerkin scheme allows a fast solution of the respective Poisson equations (for either pressure or streamfunction,

depending on the formulation of the basic equations employed) that have to be solved at each time step. In order to further reduce the computational expense, we used a simple adaptation strategy, in which at each stage of the simulation the computational box is only slightly longer than the frontal system, and is gradually enlarged as the fronts proceed. This approach is justified by the fact that boundaries in the longitudinal direction do not significantly affect the dynamics of the flow until the advancing fronts have approached the boundaries to within about 1–2 channel half-heights (see Härtel & Meiburg 1999).

While in our simulations the computational domain is always large enough to accommodate the full length of the fronts, other authors have pursued a different approach in the past. For example, Klemp *et al.* (1994) used a translating coordinate system that moves with the front and only retains its leading part in a computational box of finite size. The advantage of this treatment is that it greatly reduces the computational costs of the simulation. However, this is achieved at the expense of a substantial simplification of the problem, since the full interaction of the mutually intruding fronts is no longer captured. For example, due to both the ever increasing influence of viscous forces at the interface and the developing boundary layers, the front speed is bound to decay in a lock-exchange flow, a feature that is missed if the computational domain does not encompass the complete frontal system. In addition, difficulties with this approach arise when DNS are performed, which fully resolve the formation of interfacial vortices. The convection of these vortices out of the flow domain renders the specification of proper inflow/outflow boundary conditions difficult.

The code developed by Härtel *et al.* (1997) uses the velocity–pressure formulation (1)–(3). It employs a mixed discretization in space based on a spectral-element collocation technique in the wall-normal direction, and Fourier expansions in the longitudinal and lateral directions. For the time discretization, a semi-implicit method is employed. This semi-implicit scheme, along with the spectral-element discretization, provides good flexibility of the numerical mesh in the normal direction, but in a lock-exchange flow this flexibility is not indispensable. To reach very high Grashof numbers, we have therefore also adopted an existing highly optimized program for the simulation of two-dimensional particle-driven flows. This code is based on the above vorticity–streamfunction formulation and employs equidistant grids in both directions, along with an explicit third-order-accurate low-storage Runge–Kutta time integration scheme (see Wray 1991). Like the code of Härtel *et al.* (1997), this employs a spectral method in the longitudinal direction, which expands both the streamfunction ψ and the vorticity ω in cosine series, i.e.

$$\psi(x_1, x_3, t) = \sum_k \hat{\psi}_k(x_3, t) \cos(k\,\alpha\,x_1), \tag{16}$$

$$\omega(x_1, x_3, t) = \sum_k \hat{\omega}_k(x_3, t) \cos(k\,\alpha\,x_1). \tag{17}$$

Here

$$|k| < \frac{N_1}{2}, \quad \alpha = \frac{\pi}{L_1}, \tag{18}$$

and N_1 represents the number of grid points in the longitudinal direction. The explicit time integration, together with the Galerkin approximation in x_1, transforms (13), (14) into the following equations for the time advancement of each pair of modes

$(\hat{\psi}_k, \hat{\omega}_k)$ over the mth Runge–Kutta substep ($m = 0, 1, 2$):

$$\hat{\omega}_k^{m+1} = \hat{\omega}_k^m + \gamma^m \Delta t \left(\frac{1}{\sqrt{Gr}} \left((\hat{\omega}_k^m)'' - (k\,\alpha)^2 \hat{\omega}_k^m \right) + \hat{N}^m + \hat{f}_b^m \right)$$

$$+ \eta^m \Delta t \left(\frac{1}{\sqrt{Gr}} \left((\hat{\omega}_k^{m-1})'' - (k\,\alpha)^2 \hat{\omega}_k^{m-1} \right) + \hat{N}^{m-1} + \hat{f}_b^{m-1} \right), \quad (19)$$

$$(\hat{\psi}_k^{m+1})'' = -\hat{\omega}_k^{m+1}. \tag{20}$$

In equations (19), (20), the prime denotes differentiation with respect to x_3. $\hat{N}$ and $\hat{f}_b$ represent the coefficients of the Fourier transforms of the nonlinear term and the buoyancy term, respectively,

$$N = -u_1 \frac{\partial \omega}{\partial x_1} - u_3 \frac{\partial \omega}{\partial x_3}, \tag{21}$$

$$f_b = -\frac{\partial \rho}{\partial x_1}. \tag{22}$$

The evaluation of the nonlinearity N at each time level is performed in a pseudo-spectral manner (cf. Canuto *et al.* 1988). For the differentiation in the normal direction we employ compact finite differences in the form given by Lele (1992), which are of sixth order in the interior of the flow domain. Given all quantities at time m and $m - 1$, equations (19), (20) are then readily solved for $\hat{\psi}_k^{m+1}$ and $\hat{\omega}_k^{m+1}$. As boundary conditions at $x_3 = \pm 1$ we impose either rigid no-slip walls or slip boundaries, which, in terms of streamfunction and vorticity, are

$$\text{no-slip:} \quad \hat{\psi}_k^{m+1} = 0, \quad \hat{\omega}_k^{m+1} = -(\hat{\psi}_k^m)'', \tag{23}$$

$$\text{slip:} \quad \hat{\psi}_k^{m+1} = 0, \quad \hat{\omega}_k^{m+1} = 0. \tag{24}$$

For the density field we do not apply a Fourier scheme in x_1, since derivatives in ρ can be represented by compact finite differences in both directions without giving rise to any complications. An explicit Runge–Kutta time integration of equation (15) is then straightforward. At the boundaries $x_3 = \pm 1$ and $x_1 = \pm L_1/2$ we require the mass flux to vanish, which corresponds to homogeneous Neumann conditions for ρ:

$$\frac{\partial \rho}{\partial x_1} = 0 \quad \text{at } x_1 = \pm L_1/2, \tag{25}$$

$$\frac{\partial \rho}{\partial x_3} = 0 \quad \text{at } x_3 = \pm 1. \tag{26}$$

We have validated the code by direct comparison of the results obtained with the two programs for several different test problems, and in all cases excellent agreement was obtained. In the present study the compact finite differences program was used for the high-Gr simulations of two-dimensional flows, while the two-dimensional and three-dimensional results at low and moderate Grashof numbers were obtained with the code of Härtel *et al.* (1997). In all simulations, the flow field was initialized with fluid at rest, i.e. $u_i = 0$ everywhere (corresponding to $\psi = 0$ and $\omega = 0$). In the initial density field, constant values are prescribed in the left- and right-hand channel halves with a steep, but smooth, transient in between. This transient has the form of an error function and its steepness depends on the actual Grashof and Schmidt numbers of the flow. Details on the derivation of the initial density profile and the associated numerical resolution requirements can be found in Härtel *et al.* (1997).
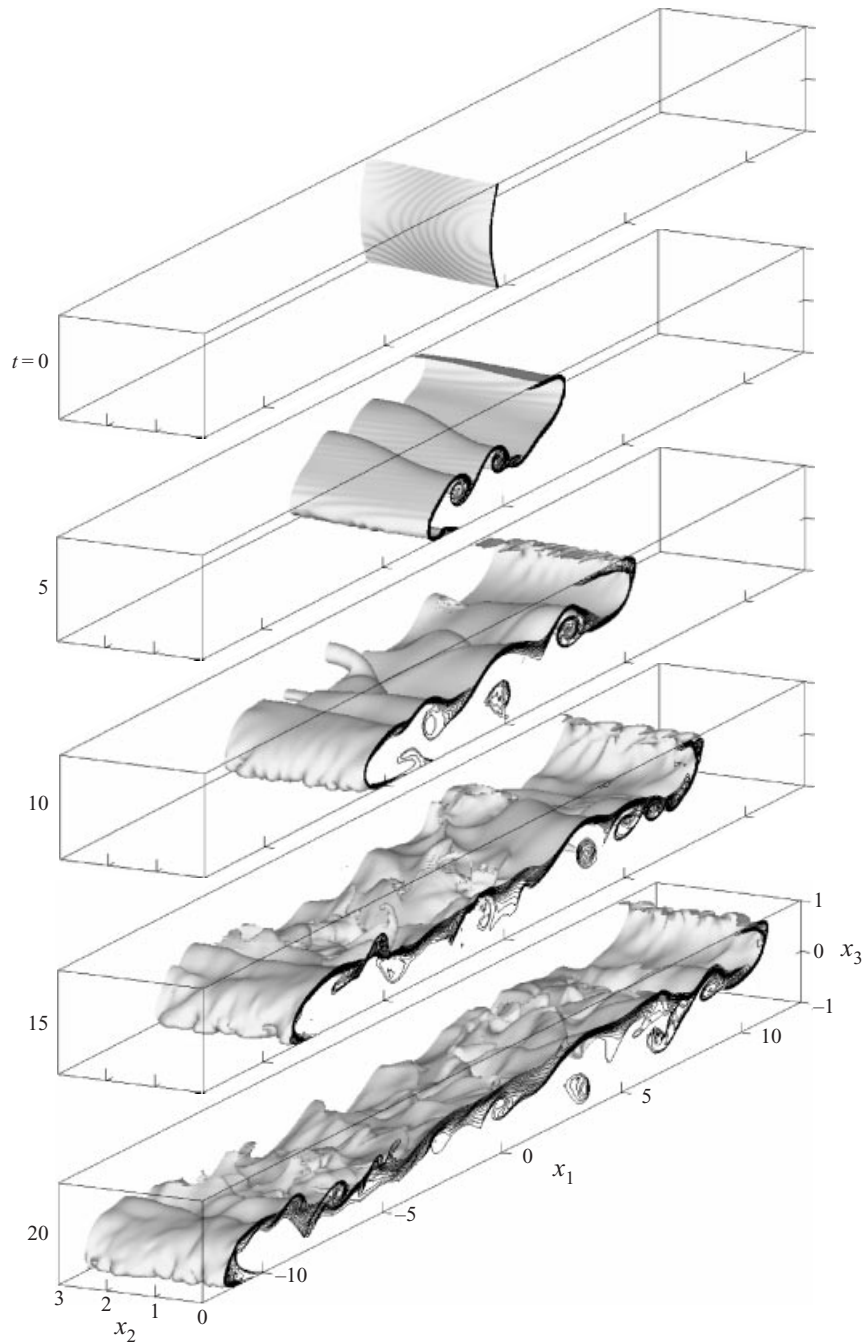
FIGURE 2. Three-dimensional lock-exchange flow between no-slip walls at a Grashof number of $Gr = 1.5 \times 10^6$ ($Sc = 0.71$). Flow fields at different times t visualized by a density isosurface for $\rho = 0.5$ together with isocontours of density in the side-plane. To enhance the breakdown to a highly three-dimensional state, the initial interface has been distorted in x_2 and x_3.

4. The no-slip case

In the following, we will briefly describe some overall features of the three-dimensional flow obtained by DNS in the light of previous experimental observations. Subsequently, we will focus on the detailed flow structure around the head of the front. In the three-dimensional simulation a computational box with a lateral size L_2 of three times the channel half-height was used, and the Grashof number was set to 1.5×10^6. This corresponds to a Reynolds number of about 750. An impression of the overall structure of the flow can be gained from figure 2. In the final stage, a computational mesh consisting of about 4.25 million grid points was used. In order to accelerate the three-dimensional breakdown, the initial density interface was somewhat distorted in the lateral and wall-normal directions. Alternatively, three-dimensional velocity disturbances could have been superimposed at time $t = 0$ in order to mimic the situation encountered in experiments, where the quick removal of the splitter plate introduces substantial turbulence at the interface. We point out, however, that the transition to a three-dimensional state does not require large-amplitude initial disturbances. A minute three-dimensionality due to round-off errors is sufficient, but the final breakdown to a fully three-dimensional flow will then occur somewhat later in time.

Clearly visible in figure 2 is the distinct head of the front with a foremost region, the so-called nose, which is raised above the wall. Also seen is the intense three-dimensionality of the flow at the leading edge, which is a typical feature of the head of a front spreading along a no-slip wall (see Simpson 1972). This lobe-and-cleft structure is absent in the simulation initially, but it evolves soon after the release. The mechanism behind the initial formation of the lobes and clefts is a buoyancy-induced instability that, as will be discussed in detail in part 2, acts in a localized fashion near the leading edge. At later times of the simulation, when the three-dimensionality at the foremost part of the front is fully developed, the average and maximum size of the lobes are about $0.5h$ and $0.9h$, respectively, which compares well with experimental data given by Simpson (1972) for this Reynolds number.

Along with the regular flow structure at the leading edge, Kelvin–Helmholtz-like interfacial vortices, which are shed from the advancing fronts, break up into three-dimensional turbulence during the later evolution of the flow. At $t = 5, 10$ the interfacial rollers still extend across the whole channel span, but their coherence has completely disappeared by time $t = 15$. However, even in a fully three-dimensional flow Kelvin–Helmholtz billows still form at the heads, although they can usually be identified in individual longitudinal cross-sections only (Simpson 1969). In the present simulation this continuing formation of interfacial billows is recognized from the density isocontours at $x_2 = 0$ which are included in figure 2.

In the two-dimensional simulations that we conducted to explore the relevant high-Gr regime, the development of small-scale three-dimensional turbulence is missing. Although a distinct head of the front develops in this case too, the break-up of both the interfacial vortices and the flow front at the leading edge is therefore precluded. For illustration, figure 3(a) shows density isocontours from a two-dimensional simulation at a Grashof number of 1.25×10^6 ($Re \approx 710$). This simulation was performed using a numerical mesh with $N_1 \times N_3 = 768 \times 91$ grid points. The striking symmetry in the density field is a direct consequence of the symmetry properties of the initial and boundary conditions, which are preserved by the Boussinesq equations. It must be stressed, however, that slight deviations from a perfectly symmetric initial state are strongly enhanced at sufficiently large Grashof numbers. From our DNS we found that for Grashof numbers beyond 10^8, say, round-off errors already suffice to obtain a visibly asymmetric solution after a few dimensionless time units.
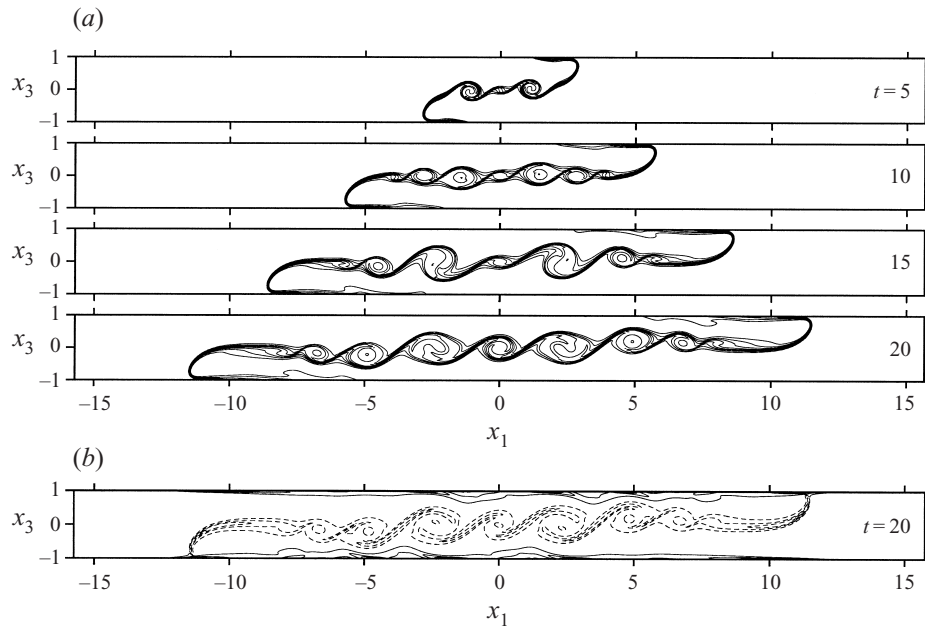
FIGURE 3. Two-dimensional lock-exchange flow between no-slip walls at a Grashof number of $Gr = 1.25 \times 10^6$. (*a*) Flow fields at various times t of the simulation visualized by isocontours of density, (*b*) isocontours of vorticity at time $t = 20$ (dashed lines $\omega < 0$, solid lines $\omega > 0$).

In figure 3(*b*) the vorticity field is given for the flow field in the bottom graph of figure 3(*a*). It shows how the (negative) vorticity generated by the baroclinic production term is contained in the interfacial region. As the flow is bounded by no-slip walls in the normal direction, the total circulation remains essentially zero throughout the simulation, and the negative vorticity at the interface is balanced by positive vorticity diffusing into the flow domain at the walls. It is recognized from figure 3(*b*) that this positive vorticity is concentrated in the boundary layers that form underneath the propagating fronts.

4.1. *Speed of the front*

In the lock-exchange configuration, the flow at the head is best analysed in a translating system that moves at the constant speed of propagation u_f which the front attains after the initial transient. In this translating system, the leading part of the front is at rest and the flow in its neighbourhood is essentially stationary. The front speed u_f is commonly defined as the speed at which the foremost point of the front travels, i.e.

$$u_f = \frac{\mathrm{d}x_1^f}{\mathrm{d}t}, \tag{27}$$

where x_1^f denotes the actual position of the foremost point in the longitudinal direction. In the analysis of our DNS data, we have determined the position of the nose by inspection of the density field from which it is most easily found. The ratio of asymptotic front velocity and buoyancy velocity is usually denoted as the Froude number Fr of the front (Simpson 1997), and is one of the most relevant integral parameters of the flow. From the Froude number and Grashof number, the Reynolds

number (8) of the front can be evaluated as

$$Re \approx 1.1 \, Fr \, \sqrt{Gr}, \tag{28}$$

where the factor 1.1 accounts for the actual height $\tilde{h}_f$ of the head, which we found to be typically some 10% larger than the channel half-height.

In the literature, there appears to exist some controversy regarding the variation of Fr with Re (or Gr) for large Reynolds numbers (see, for example, Simpson & Britter 1979). This may be at least partially due to the difficulties associated with accurately measuring the frontal velocity, which may lead to uncertainties on the order of at least several per cent (J. Müller & T. K. Fanneløp, private communication). This can make it somewhat difficult to accurately quantify the variation of Froude number with Re experimentally, especially at higher Reynolds numbers where the dependence of the front speed on viscous effects quickly diminishes. The front velocity can be determined to a much higher degree of accuracy in the present direct simulations. The relevant data are presented in figure 4, where the respective results are given from the three-dimensional DNS (open square) and a series of two-dimensional simulations with Grashof numbers ranging between 5×10^4 and 2×10^9. While a comparatively coarse computational mesh with no more than a few thousand grid points was sufficient for the two-dimensional flow at $Gr = 5 \times 10^4$, the discretization had to be increased drastically with Grashof number. Almost 10^7 grid points ($N_1 \times N_3 = 8192 \times 1200$) were used in the simulation for $Gr = 2 \times 10^9$. The range of Reynolds numbers spanned by the two-dimensional simulations extends from about 120 to 32 000. In good agreement with the experimental data given, the simulations show that the Froude number grows with increasing Grashof (or Reynolds) number over the whole range examined. It is also seen that the increase in front speed slows down at higher Grashof numbers, as mentioned before, and that the remaining increase in the high-Grashof-number regime (between $Gr = 10^8$ and 10^9, say) is indeed of the order of the typical scatter encountered in laboratory measurements. The latter is illustrated by a vertical bar in figure 4, which gives the span of results obtained in recent lock-exchange experiments. The measurement uncertainty amounts to about 5–10% in this case. Finally, we wish to point out that the agreement between the two-dimensional simulations and both the three-dimensional DNS and the experiments is remarkably close, which suggests that (at least over the range of Gr studied here) the Froude number of the front is not very sensitive to three-dimensional effects.

4.2. *Structure of the head*

For the analysis of the flow in the translating system we will use a relative coordinate x'_1, a relative velocity u'_1, and – for a two-dimensional flow – a streamfunction ψ', respectively, which are defined as

$$x'_1 = x_1 - x_1^f, \quad u'_1 = u_1 + u_f, \quad \psi' = (\psi + u_f)x_3. \tag{29}$$

A typical snapshot of the gravity-current head in the translating system is given in figure 5. The flow field is taken from the three-dimensional simulation at some later time, when the flow at the leading edge is fully developed. The pronounced lobe-and-cleft pattern at the foremost part is clearly visible from the density isosurface, and it indicates that the flow is highly three-dimensional. In the present study, however, we are primarily interested in mean properties of the three-dimensional flow, and their agreement with the corresponding properties of two-dimensional flows. In order to obtain the mean structure of the head, the flow field in figure 5 can be averaged over the full box size L_2 in the lateral direction. The resulting mean values, indicated by
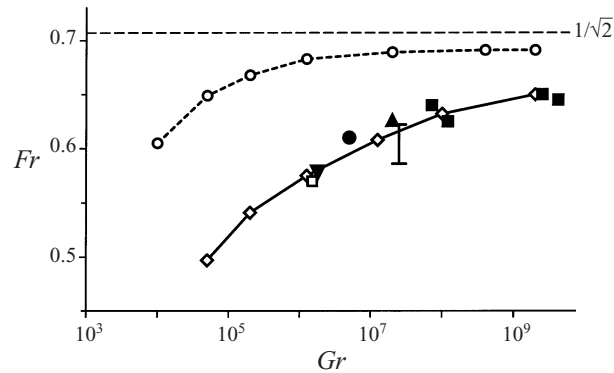
FIGURE 4. Froude number *Fr* as function of Grashof number. Results for no-slip boundaries (solid line) and slip boundaries (dashed line). Open symbols identify individual simulations. □, Three-dimensional DNS. Experimental data: ■, Keulegan (1957) (data extracted from Huppert & Simpson 1980); ●, Simpson & Britter (1979); ▲, Rottman & Simpson (1983); ▼, Keller & Chyou (1991). The vertical bar gives the span of results obtained in experiments by J. Müller & T. K. Fanneløp (private communication). $1/\sqrt{2}$ is the theoretical result of Benjamin (1968).
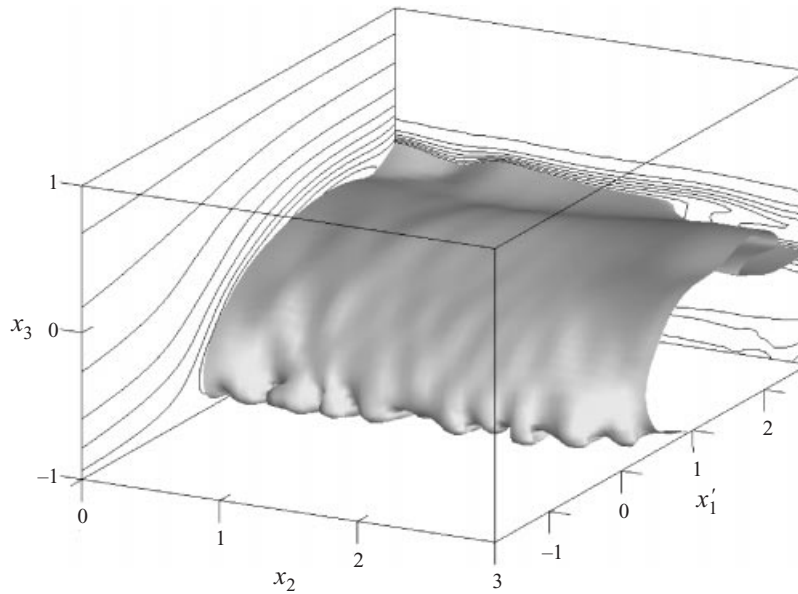
FIGURE 5. Three-dimensional lock-exchange flow at $Gr = 1.5 \times 10^6$ and $Sc = 0.71$. Flow field visualized by a density isosurface ($\rho = 0.5$). Side-plane: instantaneous streamlines in a moving frame of reference. Back plane: density distribution.

an overbar, are defined by

$$\overline{f}(x'_1, x_3, t) = \frac{1}{L_2} \int_0^{L_2} f(x'_1, x_2, x_3, t) \, dx_2, \tag{30}$$

where f can be any of the flow variables u_i, ρ, and p. Since the mean lateral velocity $\overline{u}_2$ is approximately zero, the average flow field is essentially two-dimensional and can be represented by a mean streamfunction $\overline{\psi}'$ in the translating system.
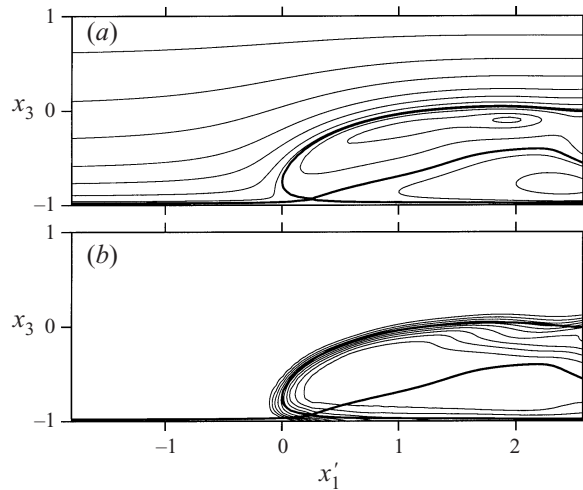
FIGURE 6. Structure of a three-dimensional gravity current head averaged in x_2 (same flow as in figure 5). (*a*) Isocontours of the average streamfunction $\overline{\psi}'$ in a moving frame of reference. (*b*) Isocontours of the average density field $\overline{\rho}$. In both graphs the thick line gives the stagnation streamline.

Isocontours of $\overline{\psi}'$ along with isocontours of the average density field $\overline{\rho}$ are given in figure 6 for the same flow field as in figure 5. A comparison of the density field of the three-dimensional flow with the two-dimensional results given in figure 3 reveals that in the three-dimensional case the average density interface is somewhat broader, as a consequence of the additional turbulent mixing between the fluids. However, in general the shape and structure of the two-dimensional front and the averaged three-dimensional front are very similar. This observation is also confirmed by a comparison of the streamline pattern of the three-dimensional simulation with the respective result for the two-dimensional flow in figure 3, which is given in figure 7.

The streamline patterns in figures 6 and 7 show that the flow of light fluid approaching the front from the left bifurcates, so that a certain fraction of it is overrun by the gravity current, while the rest ends up above the heavier fluid. In the oncoming flow, the stagnation streamline separates these two regions of the lighter fluid. Along this streamline the flow is continuously decelerated, which goes along with a substantial increase in static pressure. This is reflected by the wall-pressure distribution at $x_3 = -1$, which has been included in figure 7 in the form of a normalized pressure difference Δp_w

$$\Delta p_w = \frac{p(x_1, x_3 = -1) - p(-L_1/2, x_3 = -1)}{u_f^2/2}. \tag{31}$$

Note that for $Gr = 1.25 \times 10^6$ the increase in pressure amounts to almost two times the dynamic pressure $u_f^2/2$ of the oncoming light fluid, which highlights the substantial influence of viscous forces at low and moderate Grashof numbers.

Regarding the nature of the lobe-and-cleft instability, the topology of the streamline pattern at the head of the current, and in particular the location of the stagnation point with respect to the nose of the current, is crucial. First of all, it determines the amount of light fluid that ends up below the heavier fluid, i.e. the energy available to trigger a buoyancy-driven instability downstream of the head. In addition, it also
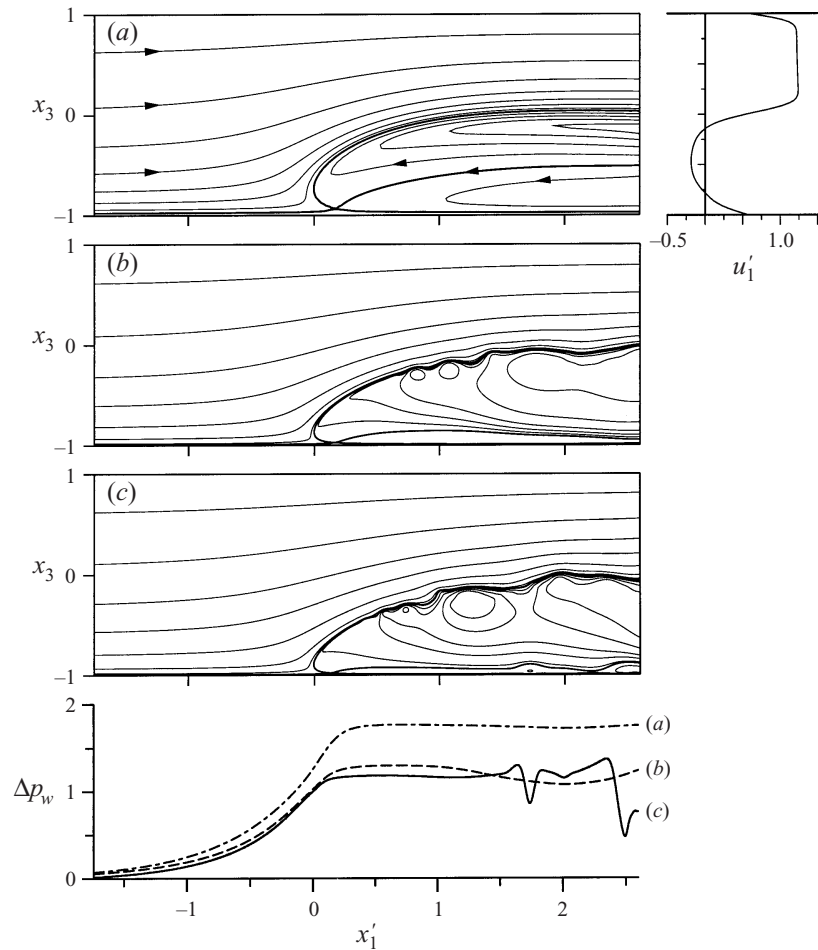
FIGURE 7. Structure of the head of a gravity-current advancing over a no-slip wall. Shown are isocontours of the streamfunction in a moving frame of reference (the thick line is the stagnation streamline). Results for $Gr = 1.25 \times 10^6$ (a), 4×10^8 (b), 2×10^9 (c). Top right: velocity profile $u'_1(x_3)$ at the right-hand margin of the section shown (note that the walls at $x_3 = \pm 1$ are moving to the right with speed u_f). Below: Increase in wall pressure p_w at $x_3 = -1$ normalized by $u_f^2/2$.

provides information on whether or not fluid can temporarily enter the region below the nose, only to flow around the nose and end up above the current. In this regard, the key observation from figures 6 and 7 is that the stagnation point of the flow is located below and slightly behind the foremost part of the front. This creates a region of unstable stratification at the leading edge that does not involve the light fluid eventually overrun by the current. This finding on the stagnation point location is in marked contrast to what has been previously suggested in the literature, namely that the stagnation point and foremost point of a front coincide (cf. Simpson 1997; Simpson & Britter 1979). That this feature is not due to the comparatively low Reynolds number of the three-dimensional simulation becomes clear from figure 7, which shows the structure of the head as obtained from two further two-dimensional simulations for substantially higher Grashof numbers, namely for $Gr = 4 \times 10^8$ and 2×10^9 (the corresponding Froude numbers and Reynolds numbers are summarized

Gr	Re	Fr	$\Delta y_n/h$	$\Delta y_s/h$	$\dot{V}_u/\dot{V}_0$ (%)
1.25×10^6	≈ 700	0.574	0.26	0.065	1.25
4×10^8	$\approx 14\,000$	0.637	0.13	0.025	0.49
2×10^9	$\approx 32\,000$	0.651	0.11	0.018	0.34

TABLE 1. Nose height Δy_n and height of the stagnation point Δy_s in a moving frame of reference. Results for different Grashof numbers. Re is the Reynolds number defined by (28), Fr is the Froude number of the front, and $\dot{V}_u/\dot{V}_0$ is the fraction of the oncoming fluid which flows underneath the front.
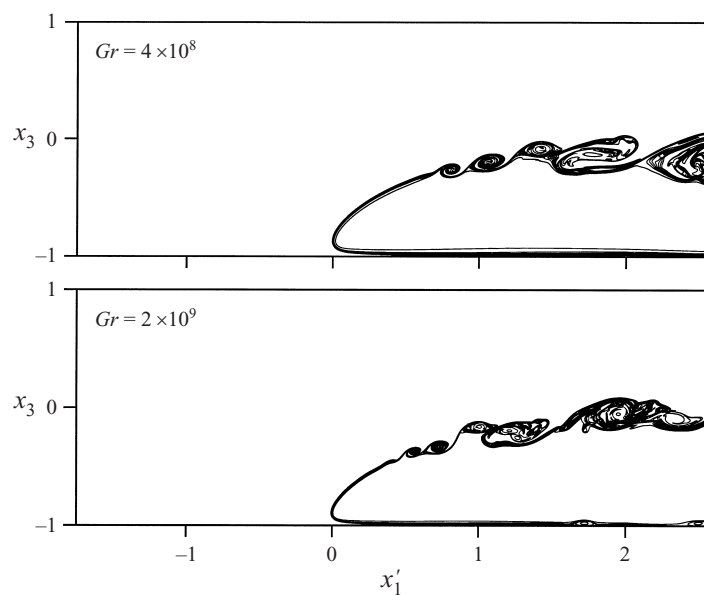

FIGURE 8. Structure of the head of a two-dimensional gravity current advancing over a no-slip wall. Flow visualized by isocontours of density. Results for different Grashof numbers.

in table 1). Due to the early vortex roll-up at the interface (see figure 8), the outline of the head in figure 7 quickly becomes corrugated at higher Gr, but the flow at the leading edge still remains steady. It is evident from the figure that the stagnation point and foremost point of the front are distinct in all cases.

Previously, the thin layer of light fluid pulled underneath the front was assumed to play the key role concerning the lobe-and-cleft instability. For this reason, we have evaluated the actual amount of light fluid $\dot{V}_u$ that flows underneath the front for the three flow fields shown in figure 7. Table 1 summarizes the results in terms of the ratio of $\dot{V}_u$ and the total volume flux $\dot{V}_0 = 2u_f$. It is seen that the volume flux of light fluid becomes extremely small at high Grashof numbers and amounts to a mere 0.3% at $Gr = 2 \times 10^9$. Its associated buoyancy therefore is very small, which already provides a hint that the lobe-and-cleft structure is not primarily driven by the fluid that is pulled beneath the current, especially since this instability is known to be more pronounced at higher Grashof numbers. Consistent with previous experimental observations, we see from our simulations that the near-wall light fluid rises slowly through the current downstream of the head, but no relation of this rise with the

frontal instability could be detected. In Part 2 we will show that the lobe-and-cleft structure, rather, develops in the unstably stratified flow region between the nose and stagnation point. The dominant mode of instability, that causes the breakdown of the two-dimensional front, is localized at the leading edge and travels with the front at speed u_f. An idea of the emergence of this instability can be gained from the flow field at time $t = 5$ in figure 2 where a small-scale disturbance at the leading edge becomes discernible, which is wave-like in the spanwise direction. The unstable modes at the leading edge are strongly amplified, and consequently their time scale is much shorter than the time scale of the buoyancy-induced rise of the thin layer of light fluid beneath the front. For $Gr = 4 \times 10^8$, for example, disturbance amplitudes may grow as fast as $\exp((4\tilde{u}_b/\tilde{h}) \times \tilde{t})$ which corresponds to a growth by a factor of about 50 in a single dimensionless time unit.

In addition to its significance for the mechanism behind the frontal instability, the location of the stagnation point is also a key ingredient in theoretical models for the flow at a gravity current head. For inviscid boundary currents or intrusive flows, the oncoming flow along the stagnation streamline is essentially loss-free, which allows the stagnation conditions to be determined by direct application of Bernoulli's theorem (see e.g. Benjamin 1968; Holyer & Huppert 1980). Simpson & Britter (1979) have tried to apply this concept to viscous boundary currents, assuming that the nose and stagnation point coincide. However, the present results not only show that these two loci are distinct, but it also becomes clear from the figures that the stagnation streamline is located in the highly rotational near-wall region which is strongly influenced by frictional forces. This precludes the application of ideal-fluid theory along the stagnation streamline, a fact that may render a refined theoretical modelling of the flow at the head difficult.

For $Gr = 1.25 \times 10^6$, the steady-state velocity profile $u'_1(x_3)$ at the right-hand margin of the section of the flow domain has also been included in figure 7 for further comparison with experiments. It is seen that the internal velocity within the advancing front exceeds the front speed. This is necessary, since at the wall and the interface there is a continuous loss of fluid from the head that must be balanced by additional transport from within the current. In figure 7 the maximum excess velocity is about 20% of the front speed, a result that again compares well with experimental data given by Simpson & Britter (1979).

A comparison of figures 6 and 7 reveals that the presence of the lobe-and-cleft structure has only a minor effect on the topology of the mean flow at the leading edge. Also, the height of the nose appears hardly affected by the three-dimensionality. From the stagnation streamline the nose elevation Δy_n, which is the distance between nose and lower wall, is estimated to lie between 0.23 and 0.24 for the three-dimensional flow, which is only some 10% smaller than the corresponding value for the two-dimensional flow at similar Reynolds number (see table 1). In addition to the nose elevation, table 1 also summarizes the elevation Δy_s of the stagnation point for all three flows shown in figure 7. It is seen that both quantities decrease with increasing Gr which again demonstrates that Grashof-number effects in the flow persist over the whole range examined. However, apart from quantitative changes they do not alter the picture qualitatively, as became clear from figure 7. A direct comparison of the data in table 1 with experimental observations is provided in figure 9, where the normalized nose height is depicted. The comparison shows that for all Reynolds numbers the two-dimensional simulations agree well with the experiments, giving further evidence that the nose elevation, similarly to the Froude number discussed in §4.1, is not affected much by the three-dimensionality of the flow.
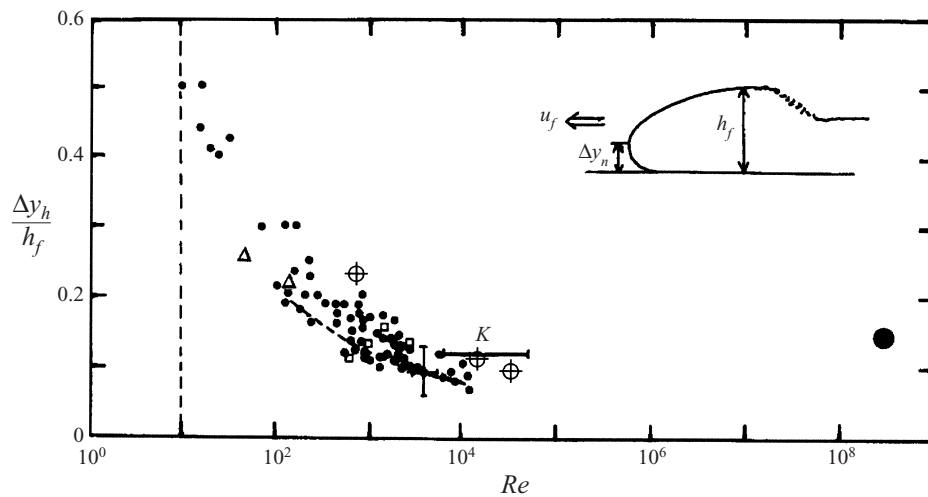
FIGURE 9. Variation of nose height Δy_n with Reynolds number (figure after Simpson & Britter 1979). Δy_n is normalized with the total head height $\tilde{h}_f$, and $Re = \tilde{u}_f \tilde{h}_f / \tilde{v}$. The dashed line is from Simpson (1972). ●, △, □, and K are from the works of Simpson & Britter (1979), Braucher (1950), Wood (1965) and Keulegan (1958); ● is an atmospheric result from Lawson (1971); ⊕ present two-dimensional DNS data.
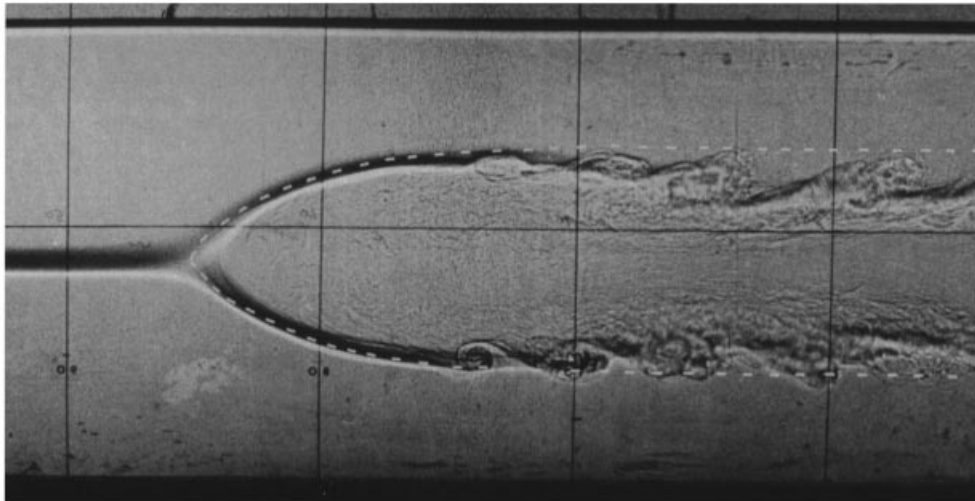

FIGURE 10. Intrusive gravity current travelling along a density interface between two fluids. The dashed lines give the front shape derived by Benjamin (1968). (Courtesy R. Britter, with permission.)

5. The slip case

Gravity currents of heavier fluid usually spread over solid boundaries underneath them, where the no-slip condition holds. In the inverse case of the dispersion of light fluid in an environment of higher density, the flow may also occur along slip boundaries, such as in the case of freshwater entering a saltwater reservoir, where it spreads along the free surface. We note that a free surface differs from a pure slip boundary in that the pressure along a slip boundary does not need to be constant, but this difference is only significant for flows with larger density variations (see

Benjamin 1968; Daly & Pracht 1968; Britter & Simpson 1978). In numerical studies of gravity currents driven by small density differences, it is common therefore to treat free surfaces as slip boundaries (cf. Kao *et al.* 1977; Wang 1985) which is also done here. In order to study directly the effect of boundary conditions on the flow, we have carried out additional two-dimensional DNS for lock-exchange flows in which slip conditions were imposed at both the upper and the lower boundary. In the laboratory, a very similar flow can be generated by means of an intrusive gravity current that travels along a thin density interface between two fluids in an open channel. As pointed out by Britter & Simpson (1981), such a flow resembles a gravity current along a slip boundary if the two fluid layers are of equal depth and the density of the intruding fluid is the mean of the two densities. Figure 10 gives a snapshot of such a flow where the (virtual) lower slip boundary coincides with the plane of symmetry defined by the density interface ahead of the front. The figure shows that the three-dimensional instability at the leading edge is absent in the slip case. Consequently, the flow at the foremost part of the front, which is of primary interest here, remains essentially two-dimensional (see also Britter & Simpson 1978). For this reason, we have not conducted a three-dimensional simulation for slip boundaries in the course of the present study.

The principal difference between dispersion along a solid wall and a slip boundary is that in the latter case no frictional forces are being exerted on the advancing front by the boundary. Surface friction may retard a propagating front substantially, as has been demonstrated in experiments and computational studies (Haase & Smith 1989; Simpson & Britter 1980; Wang 1985), and it also strongly influences the topology of the flow. As figure 10 shows (see also Simpson 1972; Britter & Simpson 1978), the foremost point of the current is located right on the boundary in the slip case, which is in contrast to the no-slip case, where it is raised above the wall. This feature is also seen in the simulation results of a two-dimensional lock-exchange flow with slip boundaries, which is visualized in figure 11 with the aid of isocontours of density and vorticity. The Grashof number of the flow in figure 11 is the same as the Grashof number of the flow in figure 3, but the differences with respect to the flow structure at the foremost part are obvious. From the density fields in figure 11, it is found that no fluid is overrun by the fronts, and also that no region of unstable stratification develops at the leading edge.

5.1. *Speed of the front*

The dependence of front speed on Grashof number as obtained from the two-dimensional simulations with slip conditions is included in figure 4, where it is seen that in this case the Froude number approaches a limit of 0.69 beyond, say, $Gr = 10^8$. This is smaller than the theoretical prediction of $1/\sqrt{2}$ of Benjamin (1968), but agrees with two-dimensional simulation results of Klemp *et al.* (1994). The curves also show that the normalized frontal speeds with no-slip boundaries are smaller than those of the free-slip case, although the differences between the two decrease with increasing Gr. For $Gr = 1.25 \times 10^6$ the difference in front speed amounts to about 20%, which is very similar to the discrepancy that Klemp *et al.* (1994) observed between their computational results for slip boundaries and the experiments of Rottman & Simpson (1983). To account for surface friction, Klemp *et al.* introduced an empirical drag coefficient assuming a turbulent boundary layer underneath the front, which led to improved agreement. However, figure 4 shows that friction by a (two-dimensional) laminar boundary layer already suffices to explain the difference in front speed, and we therefore suspect that turbulence may not have played a major role in the surface drag in Rottman & Simpson's experiments.
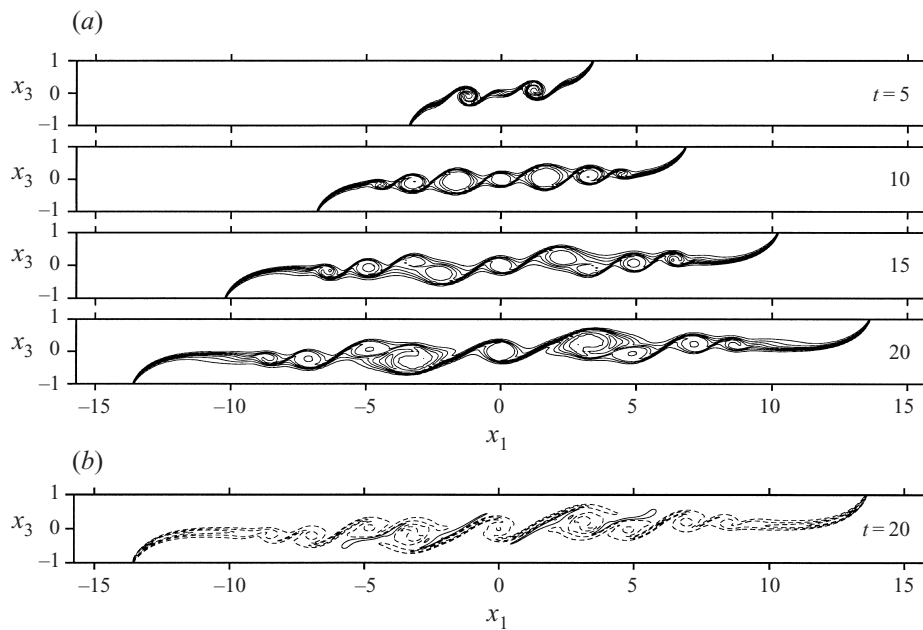
FIGURE 11. Two-dimensional lock-exchange flow between slip boundaries at a Grashof number of $Gr = 1.25 \times 10^6$. (*a*) Flow fields at various times t of the simulation visualized by isocontours of density, (*b*) isocontours of vorticity at time $t = 20$ (dashed lines $\omega < 0$, solid lines $\omega > 0$).

5.2. *Structure of the head*

Figure 12 illustrates the structure of the foremost part of the front for the slip case by instantaneous streamlines for flows at Grashof numbers of 2×10^7, 4×10^8, and 2×10^9. As in §4.2 (see equation (29)), a relative coordinate x_1' and a relative velocity u_1' in the translating system have been introduced. The corresponding Froude numbers of the fronts are $Fr = 0.689$ for the lowest Grashof number and 0.691 for the other two Grashof numbers, respectively. In all three cases, the roll-up of the interfacial vortices occurs within the section of the flow domain shown, which leads to the irregular shape of the instantaneous streamlines observed downstream of the leading edge. For dispersion along a slip boundary, the stagnation point in the translating system coincides with the foremost point of the front, and hence is located on the boundary. This is clearly seen in the streamline pattern shown in figure 12. At the stagnation point, the stagnation streamline in the interior of the flow domain meets two associated stagnation streamlines, one from within the oncoming flow and the other from within the front, which coincide with the lower boundary.

Although viscous friction does not occur at a slip boundary, friction and mixing at the interface still erode fluid from the head, and consequently some additional transport of heavy fluid from within the gravity current towards the head is required here too. As for no-slip walls, the flow in the head of the front must hence not be at rest. An idea of the magnitude of this internal transport is gained from the bottom graph in figure 12, where the relative velocity at the lower boundary $u_w' = u_1'(x_3 = -1)$ is depicted. Being identical to u_f far ahead of the front, u_w' continuously decreases to zero as the stagnation point is approached. Within the foremost part of the front u_w' is negative and almost constant, taking a value of approximately 30% of u_f. Note that the increase in u_w' at the stagnation point is very steep when the stagnation
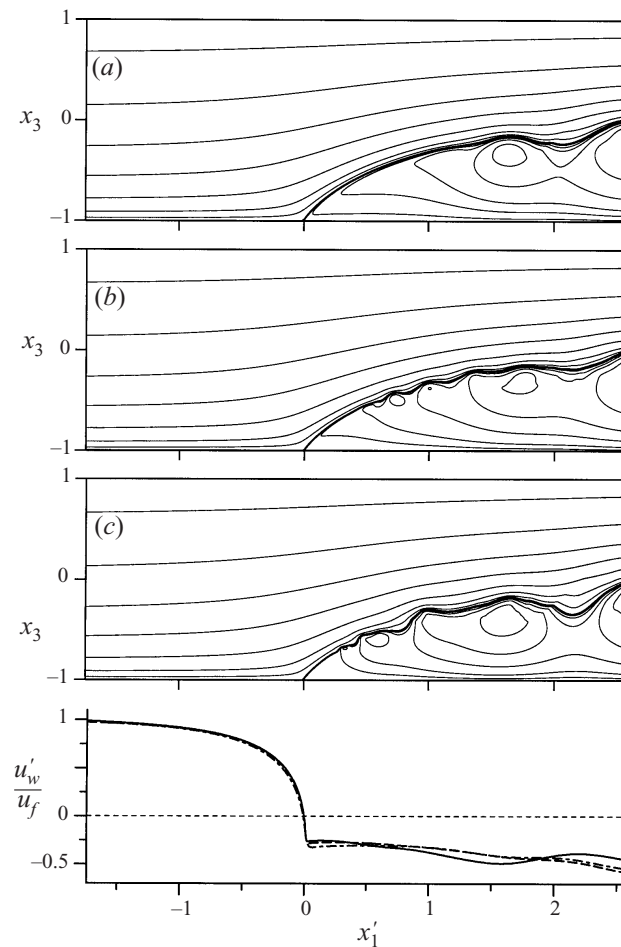
FIGURE 12. Structure of the head of a gravity-current advancing over a slip boundary. Shown are isocontours of the streamfunction in a moving frame of reference (the thick line is the stagnation streamline). Results for $Gr = 2 \times 10^7$ (a), 4×10^8 (b), 2×10^9 (c). The bottom graph shows the longitudinal velocity u'_w at the wall normalized by u_f. $-\cdot-\cdot-$, $Gr = 2 \times 10^7$; $-\,-\,-$, 4×10^8; ———, 2×10^9.

point is approached from the right. Since the flow around the leading edge of the front is stationary and essentially irrotational (except for the immediate vicinity of the stagnation point), u'_w also allows the pressure distribution $p_w(x'_1)$ at the wall to be assessed. From a straightforward application of Bernoulli's theorem, one obtains that beneath the head p_w falls some 10% below the stagnation pressure $u_f^2/2$.

In the simulations in figure 12, the flow within and around the head differs in several respects from the idealized configuration that Benjamin (1968) analysed in his theoretical work. However, it is of interest to examine the extent to which his findings may apply to the present case. Major differences between the flow considered by Benjamin and the present free-slip case are due to the developing instability at the interface and the action of frictional forces within the fluid. Also, as pointed out before, in a moving frame of reference the fluid within the advancing fronts is not stagnant, as assumed in Benjamin's analysis, and its inertia therefore cannot be neglected in the respective momentum balance. For comparison with Benjamin's result we employ the stagnation streamline, which is identical to the shape contour within the stationary
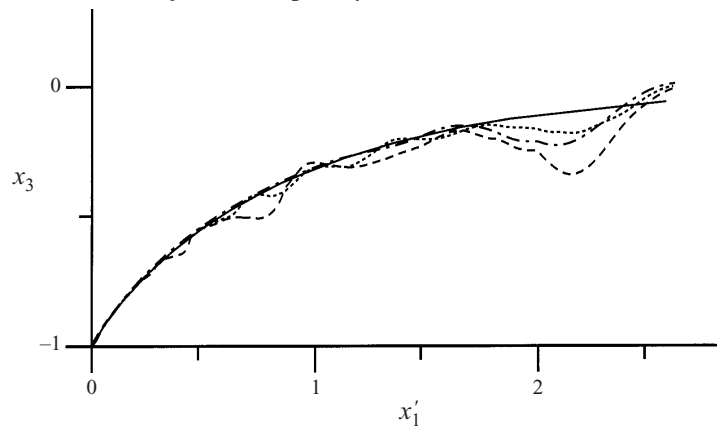
FIGURE 13. (Instantaneous) front shape of gravity currents advancing over slip boundaries (same flow fields as in figure 12). Results for $-\cdot-\cdot-$, $Gr = 2 \times 10^7$; $---$, 4×10^8; ———, 2×10^9. The solid line shows the front given by Benjamin (1968).

part of the flow at the leading edge. Figure 13 depicts the three respective stagnation streamlines from figure 12 plotted in one diagram along with the contour line given by Benjamin. It is seen that for all three Grashof numbers the stationary part of the respective stagnation streamlines (which is the part not yet distorted by the developing instability) is in almost perfect agreement with the theoretical result. Similarly good agreement with Benjamin's theory is seen in the experimental photograph in figure 10, where the theoretical contour is represented by dashed lines.

While the foremost part of an advancing front reaches a steady state soon after the initial release, the flow downstream of the leading edge may need considerably more time before it is fully developed. In order to determine the length of the head and the minimum height of the interface in its wake, we have conducted a simulation over more than 50 dimensionless time units, from which we evaluated a virtual height H of the gravity current by vertically integrating the non-dimensional density field and dividing by the full channel height, i.e.

$$H(x_1) = \tfrac{1}{2} \int_{-1}^{+1} \rho \; \mathrm{d}x_3. \tag{32}$$

This is similar to the method used by Crook & Miller (1985) and Klemp *et al.* (1994) in their analysis of numerical simulation data of two-dimensional gravity currents. The results for H obtained from five individual flow fields are given in figure 14, along with the average over the time interval $t = 40$–50, which is included as a thick solid line. If we take the head to be the region between the stagnation point and the location of minimum height of the dense layer, the length of the head amounts to about 5–$8h$ which compares well with what is seen in visualizations of laboratory flows (see, for example, Rottman & Simpson 1983). The minimum height of the current in the wake amounts to approximately 0.25 to 0.3 in figure 14, a result that again closely agrees with data reported by other authors (cf. Klemp *et al.* 1994; Simpson & Britter 1979).

6. Concluding remarks

In the present paper, we have discussed results from a direct numerical simulation study of gravity currents in two- and three-dimensional lock-release flows. The main objective of the study was a detailed analysis of the flow topology at the foremost
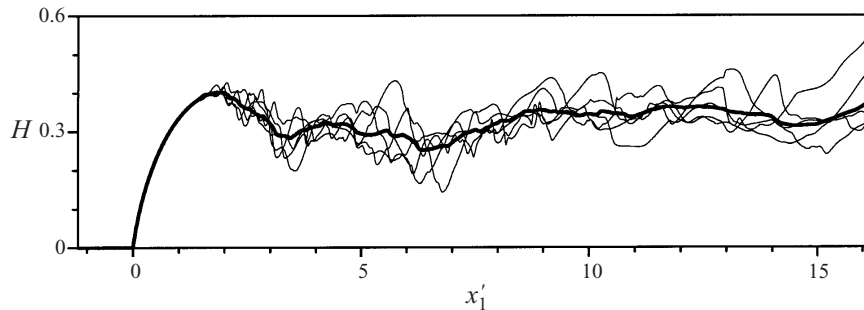
FIGURE 14. Height H (see equation (32)) of a gravity current as a function of relative coordinate x'_1. Two-dimensional simulation performed with slip boundaries and $Gr = 2 \times 10^7$. Shown are results for five time instants between $t = 40$ and 50. The thick line is the average over that time span.

part of a gravity current head, where so far no detailed information has been available from either measurements or computations. First, a careful analysis of this flow region is essential for the understanding of the pronounced lobe-and-cleft structure that develops at the leading edge of fronts spreading along solid boundaries; moreover, knowledge about the flow topology at the leading edge is also required for any refined theoretical approach to the flow at a gravity current head. In the present study two different cases were considered, namely dispersion over a rigid no-slip wall and dispersion along a slip (i.e. shear-stress free) boundary. For the simulations, high-order numerical schemes were employed which allow all relevant length and time scales in the flow to be resolved accurately.

We have presented a three-dimensional simulation which exhibits all the features that are typically observed with laboratory lock-exchange flows, including the lobe-and-cleft structure which had not been resolved in previous simulations by other authors. The simulation was performed for a Reynolds number of about 750, which is close to the upper limit of what is accessible to three-dimensional DNS with today's computer capabilities. In order to explore the high-Reynolds-number regime that is more relevant in practice, we also conducted two-dimensional simulations over a wider range of Reynolds numbers in addition to the three-dimensional simulation. However, since a two-dimensional model misses the pronounced three-dimensional instabilities of gravity currents, a careful validation of the two-dimensional results by comparison with both laboratory observations and the three-dimensional simulation at lower Reynolds number was undertaken. It was demonstrated that a two-dimensional model can reliably predict not only integral quantities such as the Froude number, but also more subtle aspects of the flow, such as the elevation of the nose or details of the flow structure within the gravity-current head.

A key finding of the present study is that for the no-slip case the flow topology at the head is different from what has been assumed previously. We have shown that in a translating system moving with the front, the stagnation point and foremost point do not coincide. Rather, the stagnation point is located upstream of the foremost point, in the vicinity of the wall. Among other things, this finding has relevance for the mechanism behind the lobe-and-cleft structure at the leading edge, since between nose and stagnation point a region of unstable stratification exists which does not involve the light fluid pulled beneath the front. The three-dimensional simulation showed that the frontal breakdown originates in this region and not, as assumed in the past, from the buoyancy-induced rise of light fluid overrun by the front. In part 2 of the present investigation we will address this point in more detail, when

we examine the stability properties of the flow at the leading edge by means of a linear-stability analysis.

For the slip case, we compared the flow topology with the theoretical result given by Benjamin, and an almost perfect agreement with respect to the shape of the front was obtained. A comparison with previously unpublished experimental results of R. E. Britter showed that such an agreement can also be observed in the closely related problem of an intrusive front travelling along a density interface. It should be stressed, however, that such good agreement is not necessarily to be expected, since in Benjamin's analysis viscosity or the presence of interfacial instabilities are not taken into account. The latter lead to a continuous loss of material from the head of the front, which implies that, in contrast to Benjamin's model, the flow within the head cannot be stagnant, since additional transport towards the head is needed to balance the losses.

In good agreement with experimental observations, the present simulations have shown that in lock-exchange flows quantitative Reynolds-number effects may persist up to Reynolds numbers of at least 30 000, i.e. throughout the typical range of laboratory experiments. On the other hand, the key findings concerning the flow topology at the foremost part do not depend on Reynolds number. We have shown that for the no-slip case the Froude number increases with increasing Reynolds number over the whole range examined, whereas it becomes independent of Reynolds number above $Re \approx 15\,000$ for slip boundaries. The maximum Froude number that a lock-exchange front may attain in the slip case is about 0.69, which is smaller than the theoretical result of $1/\sqrt{2}$ given by Benjamin. A direct comparison of simulation results for the slip and no-slip cases illustrates that wall friction retards a front considerably at low and moderate Reynolds numbers.

REFERENCES

BENJAMIN, T. B. 1968 Gravity currents and related phenomena. *J. Fluid Mech.* **31**, 209–248.

BRAUCHER, E. 1950 Initial characteristics of density current flow. MIT Thesis.

BRITTER, R. E. & SIMPSON, J. E. 1978 Experiments on the dynamics of a gravity current head. *J. Fluid Mech.* **88**, 223–240.

BRITTER, R. E. & SIMPSON, J. E. 1981 A note on the structure of the head of an intrusive gravity current. *J. Fluid Mech.* **112**, 459–466.

CANUTO, C., HUSSAINI, M. Y., QUARTERONI, A. & ZANG, T. A. 1988 *Spectral Methods in Fluid Dynamics*. Springer.

CROOK, N. A. & MILLER, M. J. 1985 A numerical and analytical study of atmospheric ondular bores. *Q. J. R. Met. Soc.* **111**, 225–242.

DALY, B. J. & PRACHT, W. E. 1968 Numerical study of density-current surges. *Phys. Fluids* **11**, 15–30.

FANNELØP, T. K. 1994 *Fluid Mechanics for Industrial Safety and Environmental Protection*. Elsevier.

GEBHART, B., JALURIA, Y., MAHAJAN, R. L. & SAMMAKIA, B. 1979 *Buoyancy-Induced Flows and Transport*. Hemisphere.

GRÖBELBAUER, H. P., FANNELØP, T. K. & BRITTER, R. E. 1993 The propagation of intrusion fronts of high density ratios. *J. Fluid Mech.* **250**, 669–687.

HAASE, S. P. & SMITH, R. K. 1989 The numerical simulation of atmospheric gravity currents. part I: neutrally-stable environments. *Geophys. Astrophys. Fluid Dyn.* **46**, 1–33.

Hallworth, M. A., Huppert, H. E., Phillips, J. C. & Sparks, S. J. 1996 Entrainment into two-dimensional and axisymmetric turbulent gravity currents. *J. Fluid Mech.* **308**, 289–311.

Härtel, C., Carlsson, F. & Thunblom, M. 2000 Analysis and direct numerical simulation of the flow at a gravity-current head. Part 2. The flow-front instability. *J. Fluid Mech.* **418**, 213–229.

Härtel, C., Kleiser, L., Michaud, M. & Stein, C. F. 1997 A direct numerical simulation approach to the study of intrusion fronts. *J. Engng Maths* **32**, 103–120.

Härtel, C. & Meiburg, E. 1999 Gravity currents and their analysis by direct numerical simulation. Progress Rep. 7–366. VDI, Düsseldorf.

Härtel, C., Meiburg, E. & Necker, F. 1999 Vorticity dynamics during the start–up phase of gravity currents. *Il Nuovo Cimento C* **22**, 823–833.

Holyer, J. Y. & Huppert, H. E. 1980 Gravity currents entering a two-layer fluid. *J. Fluid Mech.* **100**, 739–767.

Huppert, H. E. 1982 The propagation of two-dimensional and axisymmetric viscous gravity currents over a rigid horizontal surface. *J. Fluid Mech.* **121**, 43–58.

Huppert, H. E. 1986 The intrusion of fluid mechanics into geology. *J. Fluid Mech.* **173**, 557–594.

Huppert, H. E. & Simpson, J. E. 1980 The slumping of gravity currents. *J. Fluid Mech.* **99**, 785–799.

Jacobsen, Ø. & Magnussen, B. F. 1987 3-D numerical simulation of heavy gas dispersion. *J. Haz. Mater.* **16**, 215–230.

Kao, W. K., Park, C. & Pao, H.-P. 1977 Buoyant surface discharge and small-scale oceanic fronts: a numerical study. *J. Geophys. Res.* **82**, 1747–1752.

Keller, J. J. & Chyou, Y.-P. 1991 On the hydraulic lock-exchange problem. *Z. Angew. Math. Phys.* **42**, 874–910.

Keulegan, G. H. 1957 An experimental study of the motion of saline water from locks into fresh water channels. *US Natl Bur. Stand. Rep.* 5168.

Keulegan, G. H. 1958 The motion of saline fronts in still water. *US Natl Bur. Stand. Rep.* 5831.

Klemp, J. B., Rotunno, R. & Skamarock, W. C. 1994 On the dynamics of gravity currents in a channel. *J. Fluid Mech.* **269**, 169–198.

Lawson, T. J. 1971 Haboob structure at Khartoum. *Weather* **26**, 105–112.

Lele, S. K. 1992 Compact finite difference schemes with spectral-like resolution. *J. Comput. Phys.* **103**, 16–42.

Parsons, J. D. & García, M. H. 1998 Similarity of gravity current fronts. *Phys. Fluids* **10**, 3209–3213.

Rottman, J. W. & Simpson, J. E. 1983 Gravity currents produced by instantaneous releases of a heavy fluid in a rectangular channel. *J. Fluid Mech.* **135**, 95–110.

Simpson, J. E. 1969 A comparison between laboratory and atmospheric density currents. *Q. J. R. Met. Soc.* **95**, 758–765.

Simpson, J. E. 1972 Effects of the lower boundary on the head of a gravity current. *J. Fluid Mech.* **53**, 759–768.

Simpson, J. E. 1997 *Gravity Currents: in the Environment and the Laboratory*, 2nd Edn. Cambridge University Press.

Simpson, J. E. & Britter, R. E. 1979 The dynamics of the head of a gravity current advancing over a horizontal surface. *J. Fluid Mech.* **94**, 477–495.

Simpson, J. E. & Britter, R. E. 1980 A laboratory model of an atmospheric mesofront. *Q. J. R. Met. Soc.* **106**, 485–500.

Thorpe, A. J., Miller, M. J. & Moncrieff, M. W. 1980 Dynamic models of two-dimensional downdraughts. *Q. J. R. Met. Soc.* **106**, 463–484.

Wang, D.-P. 1985 Numerical study of gravity currents in a channel. *J. Phys. Oceanogr.* **15**, 299–305.

Wood, I. R. 1965 Studies in unsteady self preserving turbulent flows. *University of NSW, Manly Vale, NSW Australia, Rep.* 81.

Wray, A. A. 1991 Minimal storage time-advancement schemes for spectral methods. *Preprint*.

Yao, J. & Lundgren, T. S. 1996 Experimental investigation of microbursts. *Exps. Fluids* **21**, 17–25.